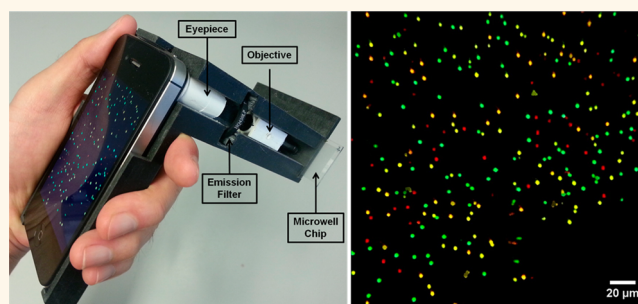


Integrated Quantum Dot Barcode Smartphone Optical Device for Wireless Multiplexed Diagnosis of Infected Patients

Kevin Ming,^{†,‡,△} Jisung Kim,^{†,‡,△} Mia J. Biondi,[△] Abdullah Syed,^{†,‡} Kun Chen,^{†,‡} Albert Lam,^{†,‡} Mario Ostrowski,[#] Anu Rebbapragada,[¶] Jordan J. Feld,[△] and Warren C. W. Chan^{*,†,‡,§,||,⊥}

[†]Institute of Biomaterials and Biomedical Engineering, [‡]Terrence Donnelly Centre for Cellular and Biomolecular Research, Departments of [§]Chemistry, ^{||}Chemical Engineering, [⊥]Materials Science and Engineering, [#]Department of Immunology, [¶]Laboratory Medicine and Pathobiology, and [△]Sandra Rotman Centre for Global Health, University of Toronto, 160 College Street, Toronto, ON M5S 3E1, Canada. [△]These authors contributed equally.

ABSTRACT Inorganic nanoparticles are ideal precursors for engineering barcodes for rapidly detecting diseases. Despite advances in the chemical design of these barcodes, they have not advanced to clinical use because they lack sensitivity and are not cost-effective due to requirement of a large read-out system. Here we combined recent advances in quantum dot barcode technology with smartphones and isothermal amplification to engineer a simple and low-cost chip-based wireless multiplex diagnostic device. We characterized the analytical performance of this device and demonstrated that the device is capable of detecting down to 1000 viral genetic copies per milliliter, and this enabled the diagnosis of patients infected with HIV or hepatitis B. More importantly, the barcoding enabled us to detect multiple infectious pathogens simultaneously, in a single test, in less than 1 h. This multiplexing capability of the device enables the diagnosis of infections that are difficult to differentiate clinically due to common symptoms such as a fever or rash. The integration of quantum dot barcoding technology with a smartphone reader provides a capacity for global surveillance of infectious diseases and the potential to accelerate knowledge exchange transfer of emerging or exigent disease threats with healthcare and military organizations in real time.



KEYWORDS: quantum dot barcode · smartphone · point-of-care · infectious disease · diagnostics · wireless · nanoparticle

The detection of diseases requires the development of technologies that can rapidly analyze genomic and proteomic targets with a single drop of biological fluid. The detection assays must be cost-effective and detect multiple targets simultaneously, which would increase accessibility and improve the speed of analysis, respectively. Ultimately, this leads to improvements in the diagnostic sensitivity and specificity and would contain the spread of diseases, especially for infectious pathogens. In the past decade, researchers have developed a wide array of barcoding structures and have demonstrated the detection of multiple biological targets in buffer. The barcodes comprise graphical,^{1,2} optical,^{3,4} or magnetic^{5,6} structures with

unique patterns that identify surface-coated biorecognition molecules that can selectively recognize biological targets of interest (e.g., whole virus, antigen, or genetic sequence). Detection occurs when a fluorescently labeled secondary targeting agent is added to the barcode, forming a sandwich structure. The code identifies the coated recognition molecule, which identifies the target, and the secondary probe confirms the presence of the disease and the quantity. The advantage of using a barcode in a diagnostic setting is that multiple targets from patient samples can be detected simultaneously, which increases the speed of analysis and improves the precision and accuracy of diagnosis. Despite advances with the chemical design of

* Address correspondence to warren.chan@utoronto.ca.

Received for review December 19, 2014 and accepted February 7, 2015.

Published online February 07, 2015
10.1021/nn5072792

© 2015 American Chemical Society

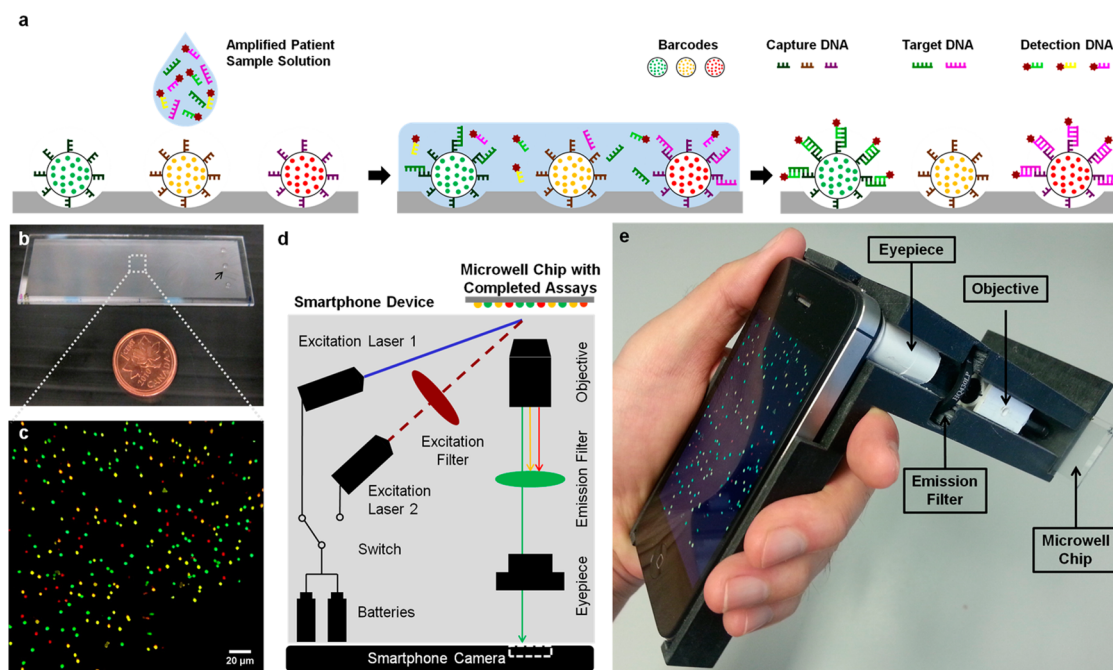


Figure 1. Overview of the smartphone device utilizing quantum dot barcodes. (a) Assay involves the addition of patient samples to a chip coated with microbeads, which are optically barcoded by quantum dots and are coated with molecules that recognize a target analyte. This target analyte joins the barcode to the secondary probe. Since each barcode is conjugated with a known biorecognition molecule for a specific pathogen target, the imaging of the optical signal from the barcode would allow for the identification of the pathogen and whether it is present in a patient sample (*i.e.*, lack of a secondary probe signal indicates no pathogen present, in this case, the yellow microbead). (b) Typical microwell chip containing different barcodes in each well. In a biological assay, we add 20 μL (for multiplexing synthetic targets) or 50 μL (for mono-infection patient samples) sample on the chip (see black arrow), incubate at 37 $^{\circ}\text{C}$ for 20–60 min, rinse, and image. (c) Smartphone camera captures the image of four different quantum dot barcodes arrayed on the surface of the chip. These barcodes are excited with a violet laser source ($\lambda_{\text{ex}} = 405 \text{ nm}$, 50 mW), and optical signals are collected by a set of lenses, filtered with 430 nm long-pass filter, and imaged using an Apple iPhone 4S smartphone with an exposure time of 0.05 s. (d) Two excitation sources excite the quantum dot barcoded chip independently. The optical emission is collected by a set of objective and eyepiece lenses, imaged using a smartphone camera, and interpreted as positive or negative detection using a custom-designed algorithm. The images may be sent wirelessly to a centralized facility for further evaluation or for the mapping and tracking of infectious diseases. (e) Image of the smartphone device.

barcodes, nanotechnology-based barcoding technologies have not advanced to patient care. The current limit of detection associated with nanotechnology-based assays (typically femto- to attomole) limits their utility for detecting most clinically relevant samples, and the read-out device remains expensive. Here, we have combined recent advances in quantum dot barcoding technology, smartphones, amplification, and software design to engineer a diagnostic device capable of detecting multiple pathogens (Figure 1) in patients with multiple blood-borne infections.

Barcodes can be engineered by infusing polystyrene beads with different emitting quantum dots.^{7,8} The quantum dots provide significant advantages over organic fluorophores for barcoding. They are brighter, have wider excitation spectra and narrower emission spectra, and are more resistant to photobleaching.^{9–11} From a device perspective, these properties are attractive because they reduce the costs of manufacturing the diagnostic device and simplify the design of the read-out system while giving high precision in identifying the optical code. This strategy also provides quantum dots with greater multiplexing capabilities,

as the use of quantum dots in a nonbarcoded detection system can reasonably differentiate only 5–6 unique signals^{10,11} versus the potentially millions in a barcode format.⁷ Furthermore, the optical signals of the quantum dots are protected in the microbead from fluorescence fluctuations as the polystyrene reduces the interaction of the quantum dots with ions, proteins, and other biological molecules.^{12,13} The microbeads are also versatile in molecular detection and can detect both genomic or proteomic targets.^{7,14,15} We have previously optimized the methods to prepare quantum dot barcodes with hundreds of distinct optical patterns and demonstrated their utility as a universal platform for detecting different panels of infectious targets using model synthetic genomic sequences.¹⁶ A critical next step is then to improve the analytical sensitivity to the zeptomole range, to design a cost-effective read-out system, and to clinically validate this technology. These are important next steps for the translation of barcoding technologies to the clinic.

We expect the barcoded device to enable clinicians to better manage the spread of diseases by improving the diagnosis of infectious pathogens, which can

spread rapidly, leading to economic burden, morbidity, and mortality. The integration of mobile cellular devices with state-of-the-art multiplexing molecular diagnostic devices would help alleviate these problems by permitting clinical diagnosis in the absence of large laboratory infrastructure, leading to more appropriate treatment, as well as enabling real-time global surveillance of infectious transmission events and predicting temporal infection trends through crowd-sourced data collection. While the concepts of smartphones have been proposed for diagnostic applications, they have primarily been used in direct imaging applications from identifying bacteria or viruses labeled with a fluorophore,^{17,18} cell counting,^{19–21} imaging the test lines on lateral flow immunoassays²² and signals from custom-made lab-on-chip assays,^{23–25} among many other approaches.^{26,27} Many of these techniques often cannot diagnose the early stages of infection because of poor analytical sensitivity. More importantly, they are incapable of detecting different strains or pathogens in a high-throughput manner due to their inability to detect multiple biomarkers simultaneously. To validate our technology, we demonstrate the ability to detect patients infected with multiple chronic blood-borne infections such as HIV and hepatitis B because these co-infections can accelerate disease progression. The diagnostic device can be extended to develop molecular testing panels for other important pathogens underlying sexually transmitted infections, malaria, influenzas A and B, and tuberculosis by simply modifying the barcode recognition molecules to the target of choice.

RESULTS AND DISCUSSION

Integration of Quantum Dot Barcoding with Smartphone Technology. A multiplex chip platform that is simple to use and can be easily transported is a main design focus of our diagnostic device. To this end, we arrayed the quantum dot barcodes on microfabricated slides with a controlled number of microbeads per unit area for detecting genetic samples (Figure 1a). Barcodes in a chip format are easier to transport than when they are in solution. Microbead arrays on a chip are currently used in sequencing analysis, but the cost of the final chip is high because the microbeads are arrayed on the ends of optical fibers.²⁸ We developed a simple method to array quantum dot barcodes on the surface of a chip. Glass slides were microfabricated with 3.0 μm diameter wells (Figure 1b). A solution of $\sim 3.0 \mu\text{m}$ sized microbead barcodes containing different combinations of fluorescence emitting CdSeS alloyed ZnS quantum dots was added to the chip. They spontaneously settled into each well, reducing overlapping and aggregation that may confound analysis of their fluorescence in later steps (Figure 1c). Once bound, these microbeads do not desorb from the surface as they are held in place by noncovalent forces. The

concentration and size of the barcodes determine the filling efficiency (Supporting Information Figure S1). The deposition of barcodes on the chip, compared to those stored in solution, enables higher portability of barcodes and reduces the number of steps in the quantum dot barcode assay process. The device is also portable and easy to use (Figure 1d, e). The components—batteries, switch, laser diodes, lenses, and filters—and 3D-printed plastic chassis are all lightweight and able to fit in one hand. The two laser diodes are switched on independently *via* a manual switch: excitation laser 1 (405 nm) excites the barcodes, and excitation laser 2 (650 nm) excites the secondary label with a filter ($\lambda_{\text{ex}} = 655/15 \text{ nm}$) that controls the wavelength excitation observed by the chip. The eyepiece and moveable objective lens magnify and focus barcodes on the chip to allow them to be viewable clearly by the naked eye on the smartphone display. The smartphone camera, in this case Apple's iPhone 4S, then captures that view. A total of five images are acquired for each sample, corresponding to each of the five emission filters ($\lambda_{\text{em}} = 430\text{LP}$, 530/10 nm, 580/10 nm, 640/10 nm, and 692/40 nm). Specifically, the 430LP filter image is used for extracting the location and size of the barcodes in the camera field of view; the 530/10 nm, 580/10 nm, and 640/10 nm filter images isolate quantum dot signals to determine barcode signatures; and the 692/40 nm filter image isolates the secondary label signal to determine the presence of target analyte bound to the barcode surface. While quantum dot barcode differentiation using a long-pass emission filter (*i.e.*, $\lambda_{\text{em}} = 430\text{LP}$ filter image) is possible when the barcode colors are few and distinct (*e.g.*, “green”, “yellow”, “red”), it becomes increasingly difficult and prone to errors when higher multiplexing is desired because the differentiation is dependent heavily on the algorithm design. To reduce the discrimination strain on the algorithm, a solution would be to develop barcodes with varying mixtures of the same quantum dots. This causes some barcodes to share similar color channel intensities (Supporting Information Figure S2), increasing the possibility of false identifications. Another method, which is what we selected for this study, is to use multiple emission filters to differentiate the optical signals. While this adds components to the read-out hardware, the use of multiple filter sets would increase the accuracy of barcode discrimination. Based on the use of multiple filters, we custom-wrote an algorithm to analyze these images. The algorithm develops a histogram of the optical signal from the secondary probe of all barcodes within the sample. A threshold is established in a measurement based on the highest signal from barcodes that do not contain any of the target molecules of interest (*i.e.*, the negative control in the experiments). A graph of barcode numbers above this threshold is used to determine a positive or negative detection (Supporting Information Figure S3). We expect samples that have the target molecule of interest to have more barcodes above this

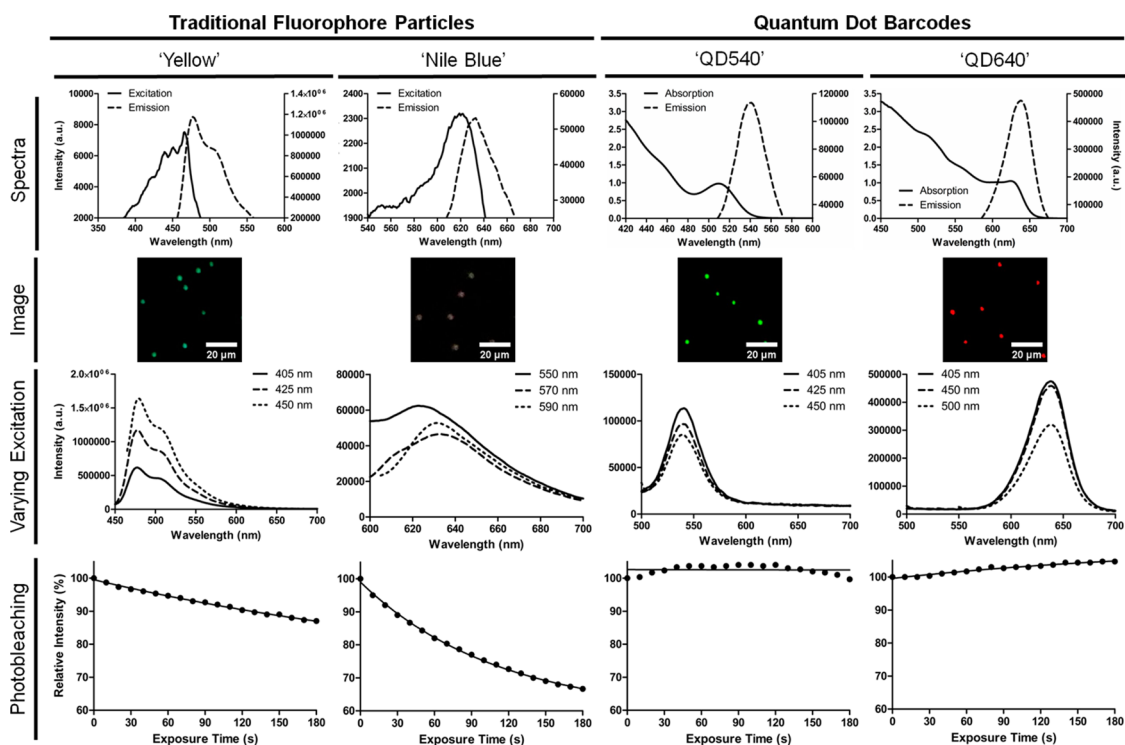


Figure 2. Comparison of the optical properties between organic dye molecules and quantum dot inside polystyrene microbeads. Polymeric particles impregnated with organic fluorophores (“Yellow” and “Nile Blue”) are compared with quantum dot barcodes (“QD540” and “QD640”): excitation/absorption and emission spectra; visual images captured by our device when excited using a 405 nm laser excitation source; emission spectra under varying excitation wavelengths; and photobleaching under continuous excitation in the device, representing the average intensities of 591, 642, 1198, and 1145 barcodes analyzed, over the 180 s duration, for “Yellow”, “Nile Blue”, “QD540”, and “QD640”, respectively.

threshold. We chose this method of analysis rather than using absolute intensity values because we found this method to obtain greater consistency in the analysis due to reduction in skewing of the measurements from a small population of microbeads. Our measurement strategy is adapted from flow cytometry, where the quantification is based on single cell counts instead of a population average. The entire imaging and analytical process takes less than 10 min and can be performed with minimal training.

Use of Quantum Dots over Traditional Fluorophores. The unique optical properties of the quantum dots for barcoding are critical for engineering a low-cost multiplex device. Here we compared the optical properties of two microbeads encapsulated with organic fluorophores (“Yellow” with $\lambda_{em} = 480$ nm and “Nile Blue” with $\lambda_{em} = 630$ nm) versus quantum dots (“QD540” with $\lambda_{em} = 530$ nm and “QD640” with $\lambda_{em} = 640$ nm). As shown in Figure 2, the quantum dots have a continuous absorption profile while the organic fluorophore has a peak-like profile (Figure 2 “Spectra”). The absorbance profile presents a significant advantage for quantum dots for engineering a point-of-care device. This would reduce the size of the final device and reduce costs as a quantum dot barcode device will only require a single energy source to excite all of the barcodes (in this case, we used a 405 nm diode laser), while the organic fluorophore barcodes will require

multiple emitting diodes or lasers to maximally excite different barcodes (Figure 2 “Image”). The quantum dot barcodes also have narrower emission profiles (e.g., full width at half-maxima of ~ 35 nm versus 60 nm for “QD540” and “Yellow”, respectively) and retain their emission peaks despite being excited by different wavelengths (e.g., “QD640” versus “Nile Blue”) (Figure 2 “Varying Excitation”). When we utilize a larger number of barcodes for greater multiplexing detection, false barcode identification would be minimized by using optical labels with narrow emission. Details of the impact of the emission profile on barcode identification are described in our previous publication.¹³ Finally, the quantum dot barcodes are much more resistant to photobleaching compared to the organic fluorophore-encapsulated barcodes (Figure 2 “Photobleaching”). This is important for accurate barcode identification as bleaching of the coded microbeads can lead to misdetection. Using quantum dots for barcoding simplifies the read-out device and reduces the costs of the final device so that it could be broadly used in the future in both resource-rich and resource-limited settings.

Synthetic Targets To Assess Device Sensitivity and Multiplexing Capability. The current detection platforms for identifying quantum dot barcodes require expensive instruments and detectors.^{14,15} Here we evaluated whether our device can differentiate the optical signals

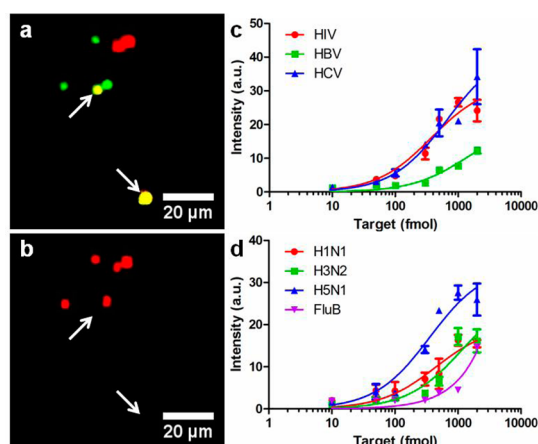


Figure 3. Visual demonstration of a barcode assay and device assay sensitivity. (a) Yellow, green, and red barcodes (identified as B_HBV, B_HCV, and B_Pos in Table 1, respectively) are deposited on the chip and imaged using the device ($\lambda_{\text{ex}} = 405 \text{ nm}$, $\lambda_{\text{em}} = 430 \text{ LP}$, exposure time = 1 s). (b) After the assay, the device-acquired fluorescence image of the microbeads bound with the target analyte and secondary probe ($\lambda_{\text{ex}} = 655/15$, $\lambda_{\text{em}} = 692/40$, exposure time = 1 s). Both green and red microbeads had positive signals. This demonstrates that their respective genomic targets are present in the sample but not for the yellow barcode. (c) Sensitivity curves for genetic biomarkers for the blood-borne viruses human immunodeficiency virus (HIV), hepatitis B virus (HBV), and hepatitis C virus (HCV), representing 8017, 7324, and 10 334 barcodes analyzed, respectively. (d) Sensitivity curves for genetic biomarkers for the influenza A viruses H1N1, H3N2, and H5N1 and influenza B virus (FluB), representing 8491, 5967, 10 182, and 4114 barcodes analyzed, respectively. All values represent the average secondary probe intensity, and error bars were calculated based on the standard deviation from three replications of each condition.

between barcodes as well as the secondary fluorescent probe used in our genetic assays. Figure 3a,b demonstrates that an iPhone camera is able to capture the distinct optical emissions of each barcode on the microwell chip, and proper filtering can differentiate the barcode optical signal from the secondary probe's signal. These studies confirmed that an iPhone camera can image barcodes on the chip surface and can be used as a detector for biological assays.

We first determine the analytical performance of the microbead-based sandwich assay using our engineered smartphone reader. We designed seven barcodes for detecting seven infectious disease biomarker targets, as shown in Table 1, plus two barcodes for the positive and negative control samples. When the target is absent (*i.e.*, negative detection), the optical signal from the microbead comprises only the quantum dot signal of the barcode. When the target is present (*i.e.*, positive detection), the microbead optical signal consists of emissions from both the quantum dots and Alexa Fluor 647 dye secondary probe. The limit of detection and linear dynamic range for each of the targets for HIV, hepatitis B virus (HBV), and hepatitis C virus (HCV), influenza type A targets H1N1, H3N2, and

H5N1, and influenza type B (FluB) (Figure 3c,d) is between 10 and 50 fmol (6×10^9 to 3×10^{10} copies) and up to 40-fold, respectively, in a final hybridization sample volume of 10 μL . This suggests that analytical performance is independent of the infectious disease targets. Note that while the dye does photobleach under continuous excitation in the device, it still retains >85% of its intensity within the first minute of excitation (Supporting Information Figure S4), the longest possible image acquisition time during our experiments, and thus should not have a significant impact on the sensitivity of detection. We can also reduce the laser power to maintain a longer signal, but this may affect the detection signal. Finally, we are also considering the use of the more photostable quantum dots as a detection probe.

Next, we demonstrated the ability to simultaneously detect multiple synthetic genetic targets from blood-borne virus panel (Figure 4). We prepared six different mock genetic samples by mixing various combinations of the genetic target sequences for each of the three pathogens of interest—HIV, HBV, and HCV—plus a positive control sequence to ensure that the barcodes are working as designed and the secondary fluorescent probe sequence. For example, we would prepare solutions that were spiked with the target sequences for HIV and positive control sequence in one combination (Figure 4b) then HIV, HBV, HCV, and positive control sequence in another combination (Figure 4f). A final hybridization sample of 20 μL was added to the chip and incubated at 37 $^{\circ}\text{C}$ for 20 min, rinsed with a washing buffer, dried, imaged, and analyzed using the algorithm. In all cases, the target sequences were correctly identified by the assay. For example, in our solution containing the sequences for HCV and positive control (Figure 4d), the bar graph shows that our technique can discriminate between barcodes bound with secondary probes (*i.e.*, HCV and positive control) *versus* those not bound (*i.e.*, HIV, HBV, and negative control). All of the probe recognition sequences for the blood-borne viral panels were carefully designed *in silico* to minimize cross-reactivity with closely related viruses using subtypes against the gag gene of HIV, core protein gene of HBV, and nucleocapsid protein gene of HCV, as per gold standard testing standards.

Clinical Validation of Diagnostic Device. We determined whether the device was capable of detecting and differentiating samples from patients with HIV and HBV from those without (*i.e.*, HIV- or HBV-negative subjects). The experiment done using synthetic targets showed that the device has a limit of detection of 10^{-15} mol, but to use the device for diagnosing patient samples, the limit of detection needed to be lowered by a factor of 10^6 . We cannot incorporate conventional PCR (polymerase chain reaction) amplification methods to our device because these PCRs are bulky and

TABLE 1. List of DNA Sequences and Their Corresponding Barcodes

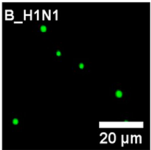
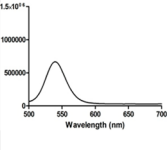
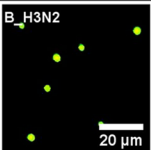
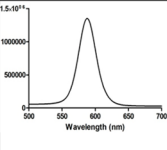
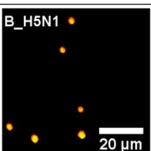
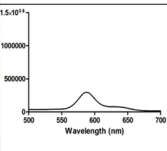
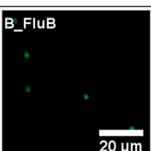
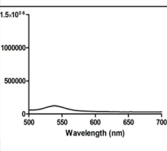
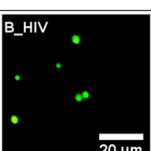
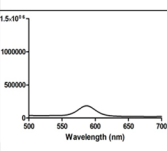
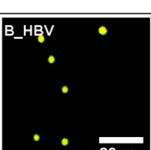
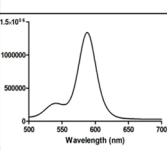
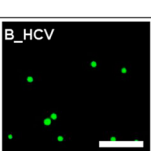
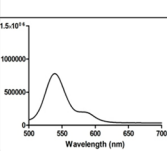
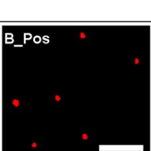
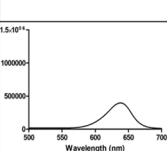
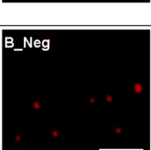
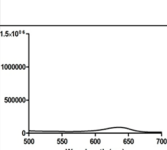
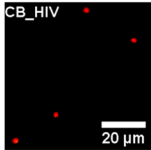
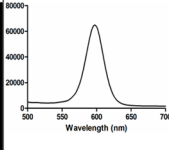
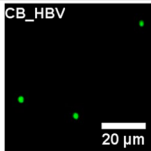
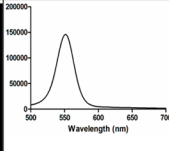
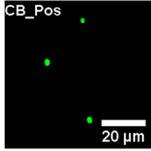
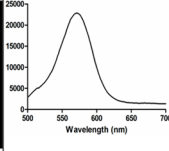
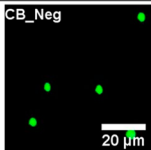
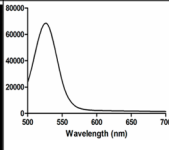
Disease/ Biomarker	Capture Name/ Sequence (5' to 3')	Target / Amplicon Name and Sequence (5' to 3')	Secondary Probe Name/ Sequence	Corresponding Barcode	Corresponding Barcode Spectrum
Influenza Hemagglutinin – Influenza Type A (H1N1)	C_H1N1 CCC TCT TAG TTT GCA TAG TTT CCC GTT ATG	T_H1N1 CGG CGA TGA ATA CCT AGC ACA CTT A CTA CA TAA CGG GAA ACT ATG CAA ACT AAG AGG G	D 5'- Alexa647- TAA GTG TGC TAG GTA TTC ATC GCC G-3'	B_H1N1 	
Influenza Neuraminidase – Influenza Type A (H3N2)	C_H3N2 ACT TGG TTG TTT GGG GGG GAG TTG AAT TCA	T_H3N2 CGG CGA TGA ATA CCT AGC ACA CTT A CTA TG AAT TCA ACT CCC CCC CAA ACA ACC AAG T		B_H3N2 	
Influenza Hemagglutinin – Influenza Type A (H5N1)	C_H5N1 CCA TTC CCT GCC ATC CTC CCT CTA TAA AAC	T_H5N1 CGG CGA TGA ATA CCT AGC ACA CTT A CTA GT TTT ATA GAG GGA GGA TGG CAG GGA ATG G		B_H5N1 	
Influenza Influenza Type B	C_FluB CAC CGC AGT TTC AGC TGC TCG AAT TGG	T_FluB CGG CGA TGA ATA CCT AGC ACA CTT A CTA CC AAT TCG AGC AGC TGA AAC TGC GGT G		B_FluB 	
Human Immuno- deficiency Virus (HIV) SK102 HIV-1	C_HIV GAG ACC ATC AAT GAG GAA GCT GCA GAA TGG GAT	T_HIV CGG CGA TGA ATA CCT AGC ACA CTT A CTA AT CCC ATT CTG CAG CTT CCT CAT TGA TGG TCT C		B_HIV 	
Hepatitis B (HBV) PB-2 – HBV	C_HBV TCA GAA GGC AAA AAA GAG AGT AAC T	T_HBV CGG CGA TGA ATA CCT AGC ACA CTT A CTA AG TTA CTC TCT TTT TTG CCT TCT GA		B_HBV 	
Hepatitis C (HCV) KY 150 – HCV	C_HCV CAT AGT GGT CTG CGG AAC CGG TGA GT	T_HCV CGG CGA TGA ATA CCT AGC ACA CTT A CTA AC TCA CCG GTT CCG CAG ACC ACT ATG		B_HCV 	
Positive Control	C_Pos GAC AAT GCT CAC TGA GGA TAG T	T_Pos CGG CGA TGA ATA CCT AGC ACA CTT A CTA AC TAT CCT CAG TGA GCA TTG TC		B_Pos 	
Negative Control	C_Neg CCA ATA TCG GCG GCC	T_Neg CGG CGA TGA ATA CCT AGC ACA CTT A CTA GG CCG CCG ATA TTG G		B_Neg 	

Table 1. continued

Disease/ Biomarker	Capture Name/ Sequence (5' to 3')	Target / Amplicon Name and Sequence (5' to 3')	Secondary Probe Name/ Sequence	Corresponding Barcode	Corresponding Barcode Spectrum
Clinical Sample HIV	CC_HIV GAA AGG TGA AGG GGC AGT AGT AAT ACA AGA C AAT AGT GAC ATA AAG GTA GTA CCA AGA AGA AAA GCA AAG ATC ATT AGG GAT TAT GGA AAA CAG ATG GCA GGT GAT GAT TGT GTG G	CT_HIV TTT TTT TTT GCC ACA CAA TCA TCA CCT GCC ATC TGT TTT CCA TAA TCC CTA ATG ATC TTT GCT TTT	CD_HIV 5'- Alexa647- TTG GTA CTA CCT TTA TGT CAC TAT TGT CTT GTA TTA CTA CTG CCC CTT CAC CTT TCC-3'	CB_HIV 	
Clinical Sample HBV	CC_HBV GGC ATG GAC ATT GAC CCT TAT AAA GAA TTT GGA GCT TCT GTG GAG TTA CTC TCT TTT TTG CCT TCT GAT TTC TTT CCG TCT ATT CGG GAC CTT CTC GAC A	CT_HBV AAA AAA AAA TGT CGA GAA GGT CCC GAA TAG ACG GAA AGA AAT CAG AAG GCA AAA AA	CD_HBV 5'-AAC TCC ACA GAA GCT CCA AAT TCT TTA TAA GGG TCA ATG TCC ATG CC- Alexa647- 3'	CB_HBV 	
Clinical Positive Control	CC_Pos GAC AAT GCT CAC TGA GGA TAG T	CT_Pos CGG CGA TGA ATA CCT AGC ACA CTT A CTA AC TAT CCT CAG TGA GCA TTG TC	CD 5'- Alexa647- TAA GTG TGC TAG GTA TTC ATC GCC G-3'	CB_Pos 	
Clinical Negative Control	CC_Neg CCA ATA TCG GCG GCC	CT_Neg CGG CGA TGA ATA CCT AGC ACA CTT A CTA GG CCG CCG ATA TTG G		CB_Neg 	

expensive. To address this issue, we optimized an isothermal amplification step, which can be performed in 10–30 min, is simple, and does not require precise temperature control.

Patient samples were collected using standard protocols, and we extracted the hepatitis B viral DNA and HIV viral RNA using magnetic microbeads. The cell membrane was first disrupted by the addition of lysis buffer, and the surface-functionalized magnetic microbeads captured viral nucleic acid. The sample was then placed in a magnetic separator to collect magnetic microbeads. Before use in our assay, the HIV RNA was reverse-transcribed into cDNA. All samples were then amplified using recombinase polymerase

amplification. The recombinase proteins were added to the isolated genetic targets to form a nucleoprotein complex, which facilitates strand transfer at the homologous sequence of the template DNA. Single-stranded binding proteins then stabilize the displaced strand of the template DNA, and the DNA polymerase extends the complementary strand.²⁹ Of the final amplified sample, 20 μ L of the double-stranded DNA was denatured and added to the chip, incubated at 37 °C, rinsed with a washing buffer, dried, imaged, and analyzed using the algorithm in a manner that is similar to detection of the synthetic targets. Figure 5a,b demonstrates the successful diagnosis of individual patient samples with HIV and HBV, respectively, of varying viral

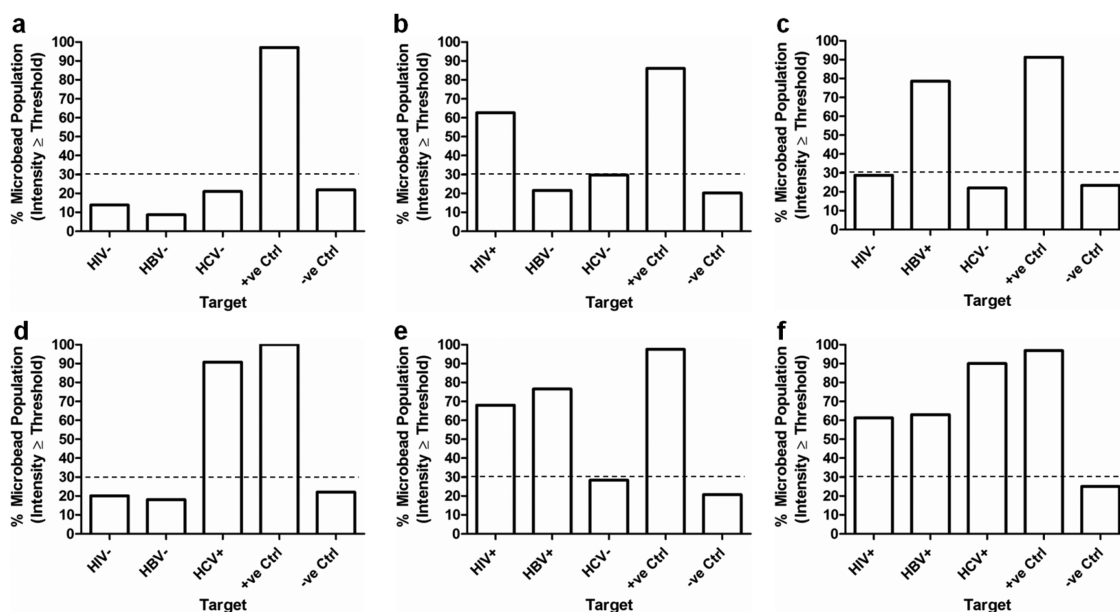


Figure 4. Multiplexed detection for synthetic target strands for the blood-borne viruses HIV, HBV, and HCV with positive and negative controls. (a) Only the positive control was present during hybridization, representing 1039 barcodes analyzed. (b) Targets for HIV and the positive control were present during hybridization, representing 1581 barcodes analyzed. (c) Targets for HBV and the positive control were present during hybridization, representing 1749 barcodes analyzed. (d) Targets for HCV and the positive control were present during hybridization, representing 1202 barcodes analyzed. (e) Targets for HIV, HBV, and the positive control were present during hybridization, representing 2401 barcodes analyzed. (f) All targets except for the negative control were present during hybridization, representing 1343 barcodes analyzed. Results represent data from three experimental replications of each condition combined into a single data set. Note that samples above the dashed 30% line are considered positive detection; otherwise, they are considered negative detection.

loads before amplification (Supporting Information Table S1). These viral loads are reported as per a clinical setting and represent a viral load range from treatment-naïve patients. They do not necessarily indicate the clinical limit of detection. The HBV-infected samples comprised multiple genotypes to ensure that our test would be widely applicable. In order to determine whether the measurement results were significant, we combined the measurements from all samples of noninfected subjects and compared them to combined measurements from the infected patients with either HIV or HBV (Figure 5c,d, respectively). Our results showed a significant difference with a p value of 0.05 and 0.01, respectively. We further confirmed the results using flow cytometry (Supporting Information Figure S5) and showed comparable outcomes. Our diagnostic device is capable of detecting viral loads in the range of 10^3 to 10^9 copies/mL and different genotypes (Supporting Information Table S1). To confirm that our device is capable of multiplex detection of patient samples, we mixed 10 μ L of each amplified patient samples containing HIV and/or HBV. We performed four-plex assays (HIV, HBV, as well as positive and negative controls), and the results clearly demonstrated that the device is capable of differentiating between the two viruses (Figure 5e–h using a smartphone device and Supporting Information Figure S6 using flow cytometry). We further investigated the level of specificity with our genetic assay by sequencing

7 HBV and 10 HIV patient samples (Supporting Information Figures S7 and S8, respectively). We found that there are 5 to 9 and 3 to 4 mismatches within HBV and HIV probe-binding regions used for the assay, respectively. Although we acknowledge that we have only used wild-type probes to detect patient samples in this study, we believe that the level of specificity can be further improved to detect single base pair mismatch by following the approach of Liong and co-workers. They used mutant probes that are designed specifically to match the mutated region and therefore bind stronger with the mutated target than the wild-type target.³⁰ The development of our device for diagnosing single-nucleotide polymorphisms was not a focus, but such studies will be a focus in future studies. Our clinical validation with real-world HBV- and HIV-infected patient samples demonstrates the effectiveness of the proposed detection platform for diagnosing infectious diseases.

CONCLUSION

All of the pathogen targets used as test panels in this study represent major infectious threats to the global community, necessitating the development of effective and innovative means for detection and informatics to identify infected individuals and accelerate clinical management. HIV, HBV, and HCV are prevalent in resource-limited settings and pose major threats to populations, often related to unknown transmission

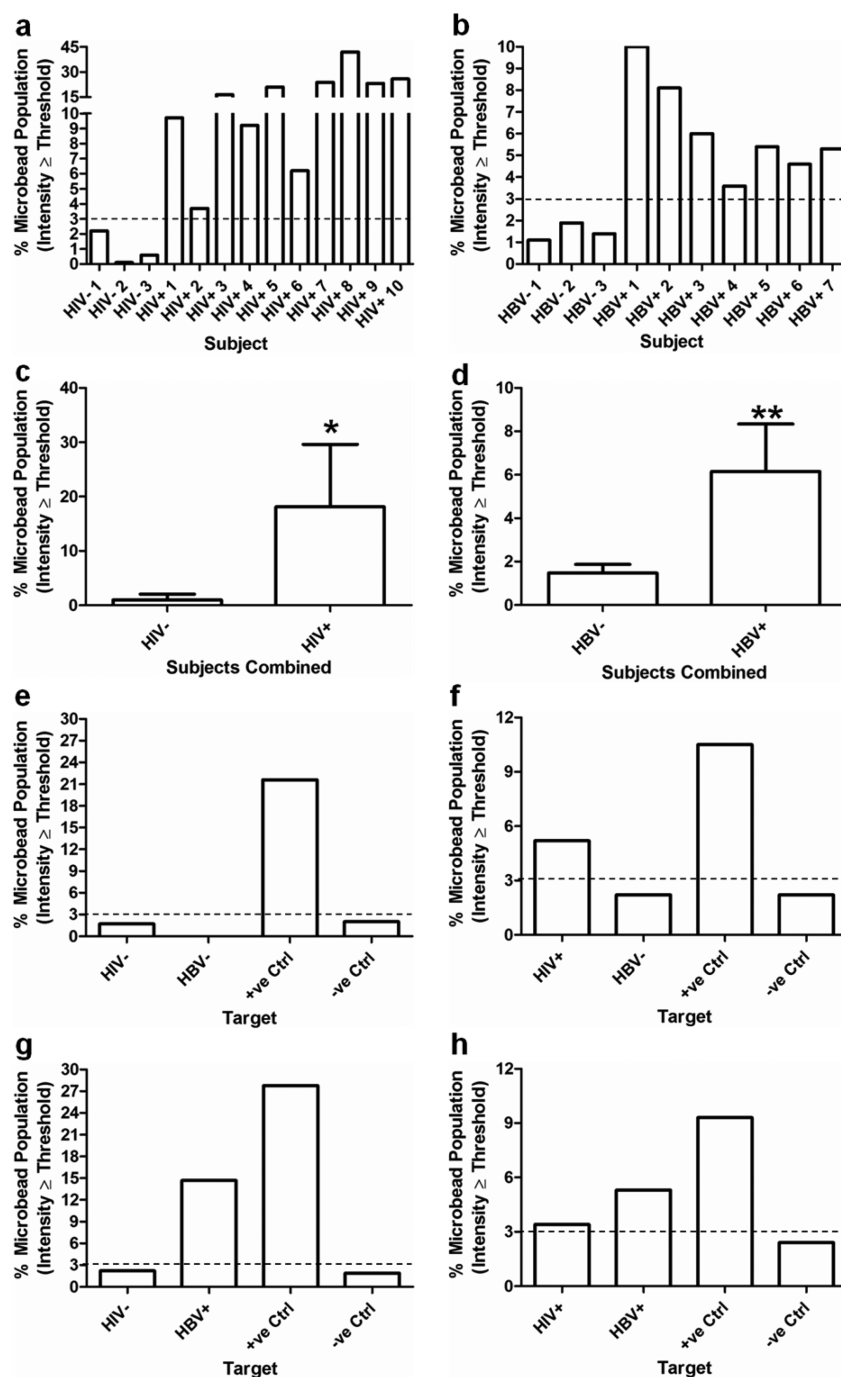


Figure 5. Detection of HIV and HBV in patient samples. (a) Detection of monoinfected amplified samples from 3 HIV-negative subjects and 10 HIV-positive patients, representing 1306, 728, 321, 1573, 626, 297, 1268, 429, 468, 499, 332, 375, and 287 barcodes analyzed, respectively, for each subject. (b) Detection of monoinfected amplified samples from 3 HBV-negative subjects and 7 HBV-positive patients, representing 361, 207, 1345, 371, 221, 1310, 806, 665, 778, and 674 barcodes analyzed, respectively, for each subject. (c) Comparison between the average combined statistics of all subjects of the HIV-negative group (3 subjects) and HIV-positive group (10 patients) from (a); error bars represent standard deviation, with statistical significance ($P < 0.05$) indicated and determined using two-sided *t*-test. (d) Comparison between the average combined statistics of all subjects of the HBV-negative group (3 subjects) and HBV-positive group (7 patients) from (b); error bars represent standard deviation, with statistical significance ($P < 0.01$) indicated and determined using two-sided *t*-test. (e–h) Detection of co-infection assays simulated with amplified HIV- and HBV-negative, as well as HIV- and HBV-positive patient samples. (e) Only positive control was present during hybridization, representing 384 barcodes analyzed. (f) HIV-positive patient sample and the positive control were present during hybridization, representing 866 barcodes analyzed. (g) HBV-positive patient sample and the positive control were present during hybridization, representing 1888 barcodes analyzed. (h) HIV- and HBV-positive patient samples and the positive control were present during hybridization, representing 1019 barcodes analyzed. Results represent data from three replications of each condition combined into a single data set. Note that samples above the dashed 3% line are considered positive detection; otherwise, they are considered negative detection. All samples were amplified. Additionally, all samples were blinded during the experiment to reduce bias.

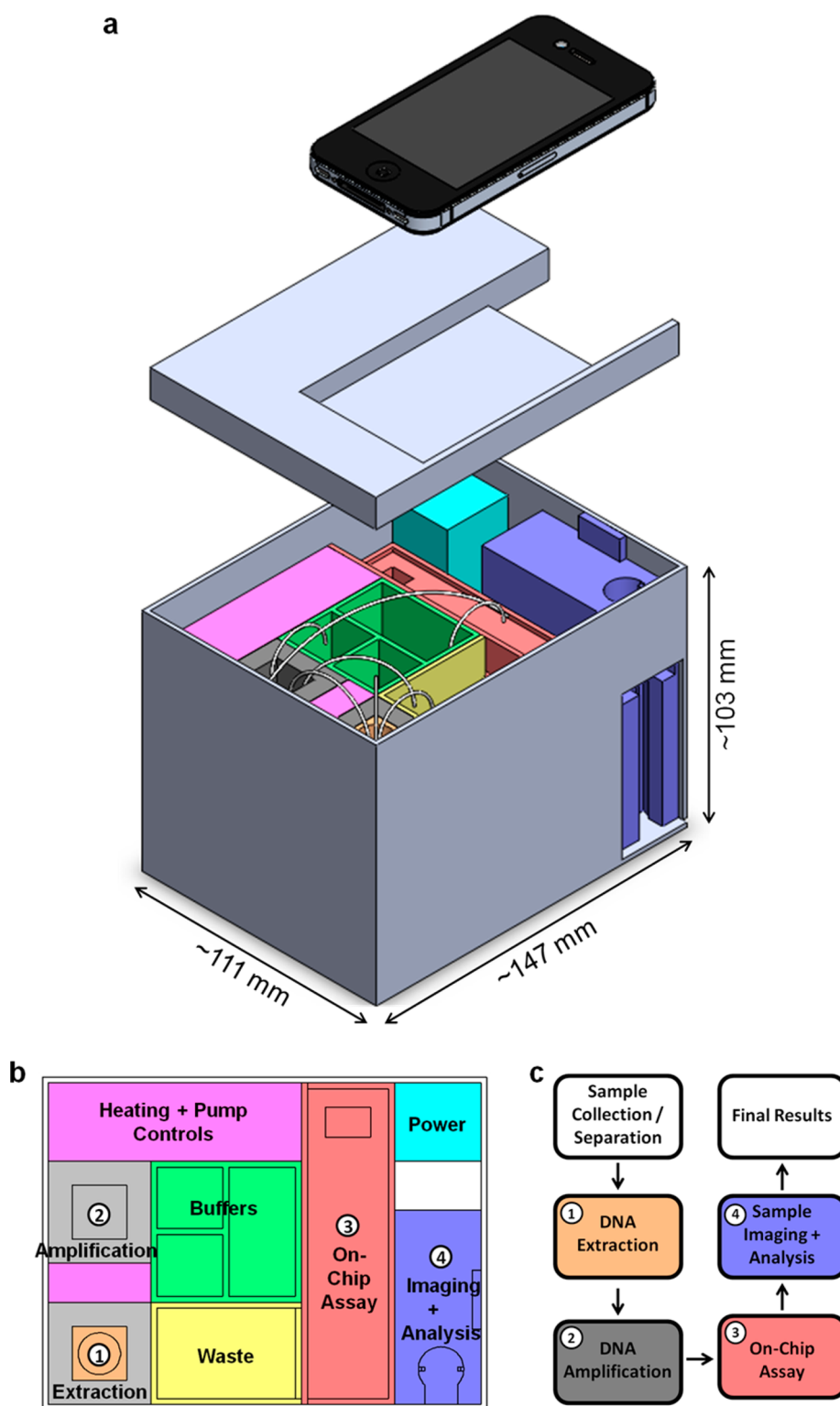


Figure 6. Integrated assembled device. (a) Visual representation of the envisioned final device, with the different compartments colored for clarity, capillary tubes to show the flow of solutions between them, and a smartphone for scale. (b) Schematics of the envisioned final device with colors matching the various compartments in (a) and numbers indicating the movement of the sample in these compartments. (c) Flow diagram illustrating the steps required for detecting pathogen targets using the envisioned final device, from patient sample to imaging and analysis, with colors and numbers matching the compartments in (a) and (b). The liquid can be moved from one compartment to the next using electrically driven flow.

through sexual contact, drug use, and contaminated blood products.^{31,32} For more rapidly spreading pathogens, immediate implementation of infection control

measures and enhanced surveillance to curb the spread of disease will be critical. Here we have shown that the integration of quantum dot barcodes with

smartphone technology can be used for multiplex molecular diagnosis of these infectious diseases with wireless transmission. There are four steps (1 through 4) and two steps (only 3 and 4) in the genetic and proteomic detection process, respectively, excluding the standard blood collection/separation processes. They are (1) extraction of the genetic target, (2) amplification of the target, (3) recognition and hybridization to barcodes on the chip and secondary probe, and (4) read-out of the chip optical signal with the smartphone followed by analysis. We believe that these two or four steps could be automated in a black box system. We envision a final black box device to all of these components, with specific chambers for each of these steps and their overall dimensions (Figure 6). Each compartment would contain disposable lyophilized samples that can be dissolved by buffers and transferred from one compartment to the next using capillaries and electrically driven flow. Building a single unit device is conventionally done as technologies advance from academic development to commercial use once each step in the process has been confirmed to work as designed. The device may also be custom-designed for different types of target molecules. For example, in the detection of a protein target, we would not need steps 1 and 2. The number of device chambers in the device can be engineered according to the target molecule. Another important aspect of the translation process is the standardization of barcode number per unit area, concentration of bioconjugated biorecognition

molecules, the dispersity of the microbeads, and the liquid volume of the assay. These parameters will increase the reproducibility of the assay in real-world applications.

This diagnostic device should be both easy to use and transportable and enable wireless transmission of diagnostics for interpretation, thus allowing the mapping, surveillance, and potential prediction of diseases in real time. The chip is highly versatile for proteomic, genomic, or whole pathogen targets.^{7,16} It may also be designed to detect different pathogen strains, coinfections, and markers of drug resistance or diagnose infections that are difficult to differentiate clinically due to shared symptoms such as a fever or rash. The only requirement will be to design panels of barcodes for each specific infectious disease agent. Future work will focus on integrating the extraction and amplification components with the existing device into a singular unit, field testing of the device, and conducting a clinical trial with greater sample size to evaluate clinical sensitivity and specificity in both the developed and developing worlds. Although we have conducted our studies using a specific brand of smartphone, the concept lends itself to further device engineering such that it can physically accommodate any cellphone or smartphone. This device can be assembled into a point-of-care unit that will enable hospitals, disease control centers, mobile units, and the military to monitor and potentially predict the onset, spread, and resistance of infectious diseases.

METHODS

Quantum Dot Synthesis. Quantum dots (CdSe alloyed ZnS capped) with a peak emission wavelength of 540 nm ("QD540") was purchased from CrystalPlex. Quantum dots with peak emission wavelengths of 515 nm ("QD515"), 547 nm ("QD547"), 560 nm ("QD560"), 589 nm ("QD589"), 596 nm ("QD596"), 615 nm ("QD615"), and 640 nm ("QD640") were synthesized and characterized according to published procedures^{33,34} and stored in chloroform at room temperature until later use.

Quantum Dot Barcode Synthesis. Quantum dot barcodes were prepared by mixing together the quantum dots (QD515, QD540, QD547, QD560, QD589, QD596, QD615, and QD640) in different ratios with a polymer-based solution (Supporting Information Tables S2 and S3). The polymer solution consisted of poly(styrene-co-maleic anhydride) (32%, cumene-terminated) from Sigma-Aldrich dissolved in chloroform, with the polymer concentration at 4 wt %. The resultant quantum dot polymer solution was then introduced into a nozzle system from Ingenia-trics using a syringe pump from Harvard Apparatus at a rate of 0.9 mL/h, as well as double-distilled (DD) water as the focusing fluid at a rate of 180 mL/h. The nozzle system was then submerged inside a beaker partially filled with DD water. The polymeric barcode microbeads were synthesized *in situ*, and the microbeads formed a white colloidal suspension in the water. After synthesis, the valve was closed and the microbeads were stabilized by overnight stirring and then collected. The microbeads were filtered using a 35 μ m BD Falcon nylon mesh strainer cap, characterized using an automated Beckman Coulter Vi-Cell counter, and stored in DD water at 4 °C until use. The quantum dot concentrations required for preparing the barcodes are presented in Supporting Information Tables S2 and S3.

Excitation, Absorption, and Emission Spectra Measurement. The excitation and emission spectra of the Yellow and Nile Blue microbeads were measured using the excitation and emission acquisition modes, respectively, on a Horiba Jobin Yvon FluoroMax-3 fluorometer. The quantum dot absorption spectra were measured using Shimadzu UV-1601PC UV-visible spectrophotometer. The quantum dot barcode emission spectra were measured using the emission acquisition mode on a Horiba Jobin Yvon FluoroMax-3 fluorometer.

Sensitivity Assay. Sensitivity assays (Figure 3c,d) were performed directly on the microwell chips for all infectious disease DNA target strands (T_H1N1, T_H3N2, T_H5N1, T_FluB, T_HIV, T_HBV, and T_HCV) and their respective conjugated barcode microbeads (B_H1N1, B_H3N2, B_H5N1, B_FluB, B_HIV, B_HBV, and B_HCV). DNA target strands from Bio Basic Inc., purchased HPLC-purified and used without further purification, were prepared in increasing concentrations of 0, 5, 10, 50, 100, 300, 500, 1000, and 2000 fmol/ μ L in TE buffer. DNA detection strand from IDT DNA Technologies with Alexa Fluor 647 on the 5' end, purchased HPLC-purified and used without further purification, was prepared with a concentration of 100 pmol/ μ L in TE buffer. Both DNA target and detection strand samples were stored at 4 °C until further use. To perform the assay, 1 μ L of the conjugated microbead sample, corresponding to approximately 10^4 conjugated microbeads, was deposited on a microwell chip for each assay condition and let dry for 1 h. Then, 1 μ L of each DNA target strand sample was mixed with 5 μ L of hybridization buffer (10 \times SSC, 0.1% SDS, heated to 60 °C), 3 μ L of DD water, and 1 μ L of DNA detection strands or DD water (for the blank condition). This resulted in a total hybridization volume of 10 μ L for each assay condition, which includes blank, 0, 10, 50, 100,

300, 500, 1000, and 2000 fmol target DNA. The hybridization solution for each assay condition was deposited over the conjugated microbead spots on the microwell chips and incubated at 37 °C for 20 min. The microwell chips were then submerged in 10 mL of washing buffer (0.5× SSC, 0.1% SDS, heated to 37 °C), washed by agitation for 20 s, then let dry for 5 min before being imaged. Note that care must be taken so that the washing buffer does not dry and crystallize over the sample spots.

Multiplexing Assay. Cross-reactivity between the blood-borne virus DNA target strands (T_HIV, T_HBV, and T_HCV) and their corresponding conjugated barcodes (B_HIV, B_HBV, and B_HCV), as well as positive and negative control cases (B_Pos and T_Pos, and B_Neg and T_Neg, respectively), was studied (Figure 4). First, 6 μL of each conjugated barcode sample, corresponding to approximately 6×10^4 barcodes each, was mixed together with 90 μL of DD water to produce a 4× dilution factor of the original. The dilution was to reduce microbead aggregation after deposition on the chip, which may confound barcode resolution during analysis. To perform the assay, 8 μL of the diluted conjugated barcode mixture, corresponding to approximately 2×10^4 conjugated microbeads, was deposited on a microwell chip for each multiplexing case and let dry for 4 h. Then, 4 μL of each target case (DD water for the negative conditions and corresponding DNA target strand sample with concentration of 2 pmol/μL for the positive conditions) was mixed with 40 μL of hybridization buffer (10× SSC, 0.1% SDS, heated to 60 °C) and 20 μL of the detection strand (concentration of 100 pmol/μL). This resulted in a total hybridization volume of 80 μL for each multiplexing case. From this, 20 μL of the hybridization solution for each multiplexing case was deposited over the conjugated barcode spots on the microwell chip and incubated at 37 °C for 20 min. The microwell chip was then submerged in 10 mL of washing buffer (0.5× SSC, 0.1% SDS, heated to 37 °C), washed by agitation for 20 s, washed again in another 10 mL of washing buffer to further reduce nonspecific binding, and then let dry for 5 min before being imaged. Note that care must be taken so that the washing buffer does not dry and crystallize over the sample spots.

Whole Blood Collection/Separation, Viral DNA/RNA Extraction, and Reverse Transcription. Whole blood was collected by venipuncture in either a Vacutainer (serum) or anticoagulant-treated tubes (plasma). Tubes were inverted several times and stood upright for 30–60 min (for serum collection). Samples were then spun in a refrigerated centrifuge, and serum or plasma was aliquoted and stored at –80 °C. HBV or HIV nucleic acid was extracted using the Chemagic Viral DNA/RNA kit (PerkinElmer), and HIV RNA was then reverse-transcribed as per the iScript cDNA synthesis kit (Bio-Rad).

Recombinase Polymerase Amplification (RPA) and Purification. RPA was performed using either extracted DNA or reverse-transcribed cDNA using the TwistAmp basic kit (TwistDx, UK). For HBV detection, a premix solution containing 0.48 pmol/μL of each forward and reverse primers (5'-GGCATGGACATTGACCCT-TATAAAGAATTTGG-3', 5'-TGTCGAGAAGGTCCCGAATAGACGG-AAAGA-3'), 9.2 μL of nuclease-free water, 29.5 μL of rehydration buffer, and 4 μL of the either extracted noninfected or infected DNA was prepared in a volume of 47.5 μL. This solution was then transferred to a tube containing the reaction pellet and mixed. The reaction was initiated by the addition of 2.5 μL of 280 mM magnesium acetate and incubated at 37 °C for 10 min to produce the 100 base pair amplicon.

For HIV detection, a premix solution containing 0.48 pmol/μL of each forward and reverse primers (5'-GAAAGGTGAAGG-GGCAGTAGTAATACAAGACA-3', 5'-CCACACAATCATCACCT GC-CATCTGTTTTCCA-3'), 11.2 μL of nuclease-free water, 29.5 μL of rehydration buffer, and 2 μL of the either extracted and reverse-transcribed noninfected or infected cDNA was prepared for a total volume of 47.5 μL. This solution was then transferred to a tube containing the reaction pellet and mixed. The reaction was initiated by the addition of 2.5 μL of 280 mM magnesium acetate and incubated at 37 °C for 30 min to produce the 116 base pair amplicon.

RPA products were purified using an EZ-10 spin column DNA gel extraction kit (Bio Basic) and eluted into 50 μL for

detection. Purified DNA was visualized by gel electrophoresis and kept at 4 °C until later use.

Monoinfection Assays Using Amplified Clinical Samples. Clinical monoinfection assays (Figure 5a–d) were performed directly on the microwell chips using HIV- and HBV-negative as well as HIV- and HBV-positive samples after amplification. DNA detection strands from IDT DNA Technologies with Alexa Fluor 647 on either the 5' end (CD_HIV) or the 3' end (CD_HBV), purchased HPLC-purified and used without further purification, for the HIV and HBV target sequences, were prepared with concentration of 100 pmol/μL in TE buffer and stored at 4 °C until further use. To perform the assay, 1 μL of the conjugated microbead sample, corresponding to approximately 10^4 conjugated microbeads, was deposited on a microwell chip for each assay condition and let dry for 1 h. During this time, 20 μL of the amplified sample was mixed with 5 μL of the corresponding detection strand and denatured at 100 °C for 15 min. Then, the 25 μL denaturation solution was mixed with 25 μL of hybridization buffer (10× SSC, 0.1% SDS, heated to 60 °C). The 50 μL hybridization solution was deposited over the dried conjugated microbead spot on the microwell chip, incubated at 37 °C for 60 min, and let cool at room temperature for 5 min. The microwell chip was then submerged in 200 mL of washing buffer (0.5× SSC, 0.1% SDS, heated to 37 °C), washed by agitation for 10 s, washed again in another 200 mL of washing buffer to further reduce nonspecific binding, and let dry for 5 min before being imaged. Note that care must be taken so that the washing buffer does not dry and crystallize over the sample spots.

Co-infection Assays Using Amplified Clinical Samples. Cross-reactivity between the amplified HIV and HBV clinical samples (CT_HIV and CT_HBV) and their corresponding conjugated barcodes (CB_HIV and CB_HBV), as well as positive and negative control cases (CB_Pos and CT_Pos, and CB_Neg and CT_Neg, respectively), was studied (Figure 5e–h). First, 5 μL of each conjugated barcode sample, corresponding to approximately 5×10^4 barcodes each, was mixed together with 20 μL of DD water to produce a 2× dilution factor of the original. The dilution was to reduce microbead aggregation after deposition on the chip, which may confound barcode resolution during analysis. To perform the assay, 1 μL of the diluted conjugated barcode mixture, corresponding to approximately 5×10^3 conjugated microbeads, was deposited on a microwell chip for each multiplexing case and let dry for 1 h. During this time, 10 μL of each amplified sample was mixed with 5 μL of each of the corresponding detection strands (5 μL of CD_HIV, 5 μL CD_HBV, and 10 μL of CD for both CT_Pos and CT_Neg) and denatured at 100 °C for 15 min. Then, the 60 μL denaturation solution was mixed with 60 μL of hybridization buffer (10× SSC, 0.1% SDS, heated to 60 °C). The 120 μL hybridization solution was deposited over the dried conjugated microbead spot on the microwell chip, incubated at 37 °C for 60 min, and let cool at room temperature for 5 min. The microwell chip was then submerged in 400 mL of washing buffer (0.5× SSC, 0.1% SDS, heated to 37 °C), washed by agitation for 10 s, washed again in another 400 mL of washing buffer to further reduce nonspecific binding, and let dry for 5 min before being imaged. Note that care must be taken so that the washing buffer does not dry and crystallize over the sample spots.

Device Design and Construction. The device was designed using SolidWorks 2012 and 3D-printed commercially (Reprodux, North York, Ontario, Canada). Laser diode excitation sources of 405 nm 50 mW (<http://www.ebay.com/itm/170719374707>) and 650 nm 50 mW (http://www.ebay.com/itm/1pcs-650-nm-50mw-Red-Laser-Diode-Dot-Module-/370650098149?pt= LH_DefaultDomain_0&hash=item564c77a9e5) were purchased online and secured into the device as delivered. The device was designed such that both lasers could excite the same spot on the chip. An excitation filter $\lambda_{ex} = 655/15$ nm (Edmund Optics) was fixed in front of the 650 nm laser diode source to reduce background signal. Both laser diodes were electrically connected to 2x AA batteries via a battery holder and single-pole triple-throw switch (both purchased from a local electronics shop) that switches between the two sources as well as an OFF state. A generic 160x–200x pocket microscope

was purchased online (<http://www.gadgetplus.ca/science/Microscope160-200x.html>). It was disassembled to extract the eyepiece and objective lenses and installed into the device manually. The eyepiece was fixed in place, but the objective was made to be movable along a track to allow focusing on the sample.

Sample Imaging. All images were acquired using the iPhone 4S from Apple (unless otherwise specified) mounted in our device. Quantum dot barcodes and Alexa Fluor 647 were excited using laser diodes with wavelengths of 405 and 650 nm, respectively. Emission filters $\lambda_{em} = 430LP$ (Thorlabs), $\lambda_{em} = 530/10$ nm (Thorlabs), $\lambda_{em} = 580/10$ nm (Thorlabs), $\lambda_{em} = 640/10$ nm (Thorlabs), and $\lambda_{em} = 692/40$ nm (Semrock, Brightline Cy5-4040A) were placed in the device's emission filter slot one at a time during imaging. The emission filter $\lambda_{em} = 430LP$ was used in conjunction with a neutral density filter OD = 1.3 (Thorlabs) to image all barcodes to determine their size and location, while avoiding intensity saturation. The emission filters $\lambda_{em} = 530/10$ nm, $\lambda_{em} = 580/10$ nm, and $\lambda_{em} = 640/10$ nm corresponded with quantum dots QD540, QD589, and QD640, respectively, and were used to isolate for their fluorescence for resolving barcodes. The emission filter $\lambda_{em} = 692/40$ nm was used to isolate for the detection strand Alexa Fluor 647 secondary label fluorescence as a means to measure the amount of analyte that hybridized with its corresponding capture strand. Image exposure times, made adjustable with the use of the NightCap app from Apple's App Store, was maintained at 1 s for all filters. In the case of fluorophore particles, they were excited using only the 405 nm laser diode source and imaged using only the emission filter $\lambda_{em} = 430LP$, the images of which were used for subsequent intensity analysis.

Image Analysis. A custom-made algorithm was written in MathWork's MATLAB for all image analysis. The algorithm accepts as inputs five emission filter images ($\lambda_{em} = 430LP$, $\lambda_{em} = 530/10$ nm, $\lambda_{em} = 580/10$ nm, $\lambda_{em} = 640/10$ nm, and $\lambda_{em} = 692/40$ nm) of a sample. The images were cropped to include microbeads of interest based on user selection. The cropped filter images were aligned with the $\lambda_{em} = 430LP$ filter image through the use of the discrete Fourier transform registration.^{35,36} The algorithm then identified the size and location of each microbead, based on its appearances in the $\lambda_{em} = 430LP$ filter image, using the Hough transform.^{37,38} Erroneously identified microbeads (e.g., debris, imaging artifacts, overlapping microbeads) were excluded based on user input. Each microbead was then associated with the mean pixel intensity across its area at each of the four remaining filter images. For each microbead, the $\lambda_{em} = 530/10$ nm, $\lambda_{em} = 580/10$ nm, $\lambda_{em} = 640/10$ nm filter image intensities comprised its intensity profile, while the $\lambda_{em} = 692/40$ nm filter image intensity indicated the fluorescent secondary probe intensity. In order to identify the microbeads on the chip, known barcode intensity profiles were first established (Supporting Information Figure S9). These profiles were obtained by imaging all the barcodes—B_H1N1, B_H3N2, B_H5N1, B_FluB, B_HIV, B_HBV, B_HCV, B_Pos, B_Neg, CB_HIV, CB_HBV, CB_Pos, and CB_Neg—alone (Table 1) and calculating the mean filter intensity across all microbeads for each filter. A microbead's intensity profile was then compared against each known barcode's intensity profile to identify the barcode of interest. Specifically, a barcode was classified according to its type (i.e., synthetic or clinical sample) and highest to lowest intensities among the filters $\lambda_{em} = 530/10$ nm, $\lambda_{em} = 580/10$ nm, and $\lambda_{em} = 640/10$ nm. This narrowed the selection down to either one barcode, in which case the barcode of interest was identified, or two barcodes. Between the two possibilities, B_{high} (with higher mean intensities) and B_{low} (with lower mean intensities), a threshold was defined for B_{low} :

$$I_{barcode} = I_{mean} + I_{STD} \quad (1)$$

where $I_{barcode}$ is the intensity threshold for B_{low} , I_{mean} is the mean intensity of B_{low} , and I_{STD} is the intensity standard deviation of B_{low} .

This threshold was calculated for the highest intensity among the three filters $\lambda_{em} = 530/10$ nm, $\lambda_{em} = 580/10$ nm, and $\lambda_{em} = 640/10$ nm for B_{low} . If the highest intensities were similar in value between B_{low} and B_{high} , the second highest filter

intensity was used. With this, if the microbead's corresponding filter intensity was equal to or lower than $I_{barcode}$, the barcode of interest was B_{low} ; otherwise, B_{high} was chosen. An example to illustrate the microbead identification process (Supporting Information Figure S10) follows.

Microbead B is imaged during a synthetic sample multiplexing test—thus classified as “synthetic sample”—has an intensity profile of [$\lambda_{em} = 530/10$ nm, $\lambda_{em} = 580/10$ nm, $\lambda_{em} = 640/10$ nm] = [4, 40, 80], so [$\lambda_{em} = 640/10$ nm] > [$\lambda_{em} = 580/10$ nm] > [$\lambda_{em} = 530/10$ nm]. On examination with the set of barcodes used for synthetic multiplexing (Supporting Information Figure S9a), B has an intensity profile (i.e., same order of highest to lowest filter intensities) similar to that of B_Pos and B_Neg. Between them, B_Neg has the lower mean intensities and thus is chosen as B_{low} with its highest filter intensity at [$\lambda_{em} = 640/10$ nm] = 30.50. Because it is much lower and thus distinguishable from B_Pos [$\lambda_{em} = 640/10$ nm] = 80.35, the intensity threshold is calculated using B_Neg [$\lambda_{em} = 640/10$ nm]:

$$I_{barcode} = I_{mean} + I_{STD} = 30.50 + 6.26 = 36.76$$

Since B [$\lambda_{em} = 640/10$ nm] = 80 is greater than $I_{barcode} = 36.76$ from B_Neg, B is identified as B_Pos.

We determined whether the analyte of interest is present by using the intensity values from the $\lambda_{em} = 692/40$ nm filter, which isolates the Alexa Fluor 647 secondary probe signal. For the synthetic sample sensitivity assays, the intensities were used directly to establish the limit of detection and dynamic range for the device. However, we used a microbead-counting method to determine the optical detection of multiplex samples and clinical samples because we achieve greater accuracy in the measurement when the measurement is based on a comparison to negative controls. Negative and positive controls are always required in analyzing complex samples, as these control samples confirm whether a technique is working as designed. When we conduct the measurements, we develop a histogram of the fluorescence intensity from the secondary probe and compare that signal to those of the negative sample. eq 2 describes this analysis.

$$Q = (\text{population of barcode whose } \lambda_{em} = 692/40 \text{ nm filter intensity } \geq I_{assay}) / (\text{total barcode population}) \quad (2)$$

That is, the barcodes whose secondary probe intensities were equal to or above the threshold I_{assay} , defined empirically, were counted, and a percentage, relative to the barcode's total population, was calculated. In the case of multiplexed detection of synthetic blood-borne viral targets (Figure 4), a detection was considered positive if $Q > 30\%$ (i.e., over 30% of said barcode had secondary probe signals above the threshold). In the case of amplified mono- and co-infected clinical samples (Figure 5), a detection was instead considered positive if $Q > 3\%$ due to their overall lower signals.

Statistics and General Methods. All data represent analysis from at least 100 barcodes to ensure that they are representative of the experimental conditions studied. The variability in the number of barcodes analyzed is due to the field of view. In some cases, there are more microbeads per field of view than others. Once we analyze >100 barcodes, the measurements were relatively consistent and did not influence the statistics. For the detection of monoinfected patient samples, we used infection-negative subject samples as a negative control, which is procedurally and clinically more accurate as negative controls than any other types of samples. To ensure clinical sample blindness, they were prepared and provided unlabeled by the collaborators (MJB, MO, and JJF) to the investigators (KM, JK, and WCWC), who then performed the experiments without knowledge of the samples' identities. Where statistical tests were necessary (i.e., comparing the infection-negative subject groups with the HIV- or HBV-infected subject groups), the two-sided *t*-test was used because the data exhibit normal distribution (e.g., Supporting Information Figure S3).

Human Subjects. The deidentified clinical samples were obtained from the Toronto Western Hospital Liver Clinic and St. Michael's Hospital biobank repository. The protocol was approved by the Research Ethics Board of the University Health

Network and St. Michael's Hospital, both affiliates of the University of Toronto. All patients provided written informed consent for storage and use of their specimens for research.

Conflict of Interest: The authors declare no competing financial interest.

Acknowledgment. W.C.W.C. acknowledges the funding support from the Collaborative Health Research Program (CHRPJ-398432 and CPG-112321), Canadian Institute of Health Research (MOP-93532), Natural Sciences and Engineering Research Council (SMFSU 459456-13 and RGPIN-288231), Ontario Ministry of Research and Innovation, and Canadian Foundation for Innovation. K.M. acknowledges Ontario Graduate Scholarship for support. J.K. and A.S. acknowledge Natural Sciences and Engineering Research Council Canada Graduate Scholarship for support. We also acknowledge Dr. Christopher Yip for insightful discussions, and Ms. Buddhisha Udagama for synthesizing the barcodes CB_HIV, CB_Pos, and CB_Neg.

Supporting Information Available: Microwell chip fill efficiency characterization, effects of continuous excitation of a secondary probe in the device, information and flow cytometry validations of our clinical sample experiments, intensity profiles, conjugation efficiencies, flow cytometry read-out of quantum dot barcodes used with clinical samples, quantum dot barcode synthesis information, and related methods. This material is available free of charge via the Internet at <http://pubs.acs.org>.

REFERENCES AND NOTES

- Appleyard, D. C.; Chapin, S. C.; Doyle, P. S. Multiplexed Protein Quantification with Barcoded Hydrogel Microparticles. *Anal. Chem.* **2011**, *83*, 193–199.
- Lee, J.; Bisso, P. W.; Srinivas, R. L.; Kim, J. J.; Swiston, A. J.; Doyle, P. S. Universal Process-Inert Encoding Architecture for Polymer Microparticles. *Nat. Mater.* **2014**, *13*, 524–529.
- Lin, C.; Jungmann, R.; Leifer, A. M.; Li, C.; Levner, D.; Church, G. M.; Shih, W. M.; Yin, P. Submicrometre Geometrically Encoded Fluorescent Barcodes Self-Assembled from DNA. *Nat. Chem.* **2012**, *4*, 832–839.
- Li, Q.; Zhang, K.; Wang, T.; Zhou, X.; Wang, J.; Wang, C.; Lin, H.; Li, X.; Lu, Y.; Huang, G. Color-Encoded Microcarriers Based on Nano-Silicon Dioxide Film for Multiplexed Immunoassays. *Analyst* **2012**, *137*, 3760–3766.
- Nam, J.-M.; Thaxton, C. S.; Mirkin, C. A. Nanoparticle-Based Bio-Bar Codes for the Ultrasensitive Detection of Proteins. *Science* **2003**, *301*, 1884–1886.
- Chung, H. J.; Castro, C. M.; Im, H.; Lee, H.; Weissleder, R. A Magneto-DNA Nanoparticle System for Rapid Detection and Phenotyping of Bacteria. *Nat. Nanotechnol.* **2013**, *8*, 369–375.
- Han, M.; Gao, X.; Su, J. Z.; Nie, S. Quantum-Dot-Tagged Microbeads for Multiplexed Optical Coding of Biomolecules. *Nat. Biotechnol.* **2001**, *19*, 631–635.
- Wang, G.; Leng, Y.; Dou, H.; Wang, L.; Li, W.; Wang, X.; Sun, K.; Shen, L.; Yuan, X.; Li, J.; et al. Highly Efficient Preparation of Multiscaled Quantum Dot Barcodes for Multiplexed Hepatitis B Detection. *ACS Nano* **2013**, *7*, 471–481.
- Alivisatos, P. The Use of Nanocrystals in Biological Detection. *Nat. Biotechnol.* **2004**, *22*, 47–52.
- Jin, Z.; Hildebrandt, N. Semiconductor Quantum Dots for *In Vitro* Diagnostics and Cellular Imaging. *Trends Biotechnol.* **2012**, *30*, 394–403.
- Kairdolf, B. A.; Smith, A. M.; Stokes, T. H.; Wang, M. D.; Young, A. N.; Nie, S. Semiconductor Quantum Dots for Bioimaging and Bidiagnostic Applications. *Annu. Rev. Anal. Chem.* **2013**, *6*, 143–162.
- Boldt, K.; Bruns, O. T.; Gaponik, N.; Eychmüller, A. Comparative Examination of the Stability of Semiconductor Quantum Dots in Various Biochemical Buffers. *J. Phys. Chem. B* **2006**, *110*, 1959–1963.
- Lee, J. A.; Hung, A.; Mardiyani, S.; Rhee, A.; Klostranec, J.; Mu, Y.; Li, D.; Chan, W. C. W. Toward the Accurate Read-out of Quantum Dot Barcodes: Design of Deconvolution Algorithms and Assessment of Fluorescence Signals in Buffer. *Adv. Mater.* **2007**, *19*, 3113–3118.
- Giri, S.; Sykes, E. A.; Jennings, T. L.; Chan, W. C. W. Rapid Screening of Genetic Biomarkers of Infectious Agents Using Quantum Dot Barcodes. *ACS Nano* **2011**, *5*, 1580–1587.
- Klostranec, J. M.; Xiang, Q.; Farcas, G. A.; Lee, J. A.; Rhee, A.; Lafferty, E. I.; Perrault, S. D.; Kain, K. C.; Chan, W. C. W. Convergence of Quantum Dot Barcodes with Microfluidics and Signal Processing for Multiplexed High-Throughput Infectious Disease Diagnostics. *Nano Lett.* **2007**, *7*, 2812–2818.
- Fournier-Bidoz, S.; Jennings, T. L.; Klostranec, J. M.; Fung, W.; Rhee, A.; Li, D.; Chan, W. C. W. Facile and Rapid One-Step Mass Preparation of Quantum-Dot Barcodes. *Angew. Chem., Int. Ed.* **2008**, *47*, 5577–5581.
- Breslauer, D. N.; Maamari, R. N.; Switz, N. A.; Lam, W. A.; Fletcher, D. A. Mobile Phone Based Clinical Microscopy for Global Health Applications. *PLoS One* **2009**, *4*, e6320.
- Wei, Q.; Qi, H.; Luo, W.; Tseng, D.; Ki, S. J.; Wan, Z.; Gorocs, Z.; Bentolila, L. A.; Wu, T.-T.; Sun, R.; et al. Fluorescent Imaging of Single Nanoparticles and Viruses on a Smart Phone. *ACS Nano* **2013**, *7*, 9147–9155.
- Zhu, H.; Mavandadi, S.; Coskun, A. F.; Yaglidere, O.; Ozcan, A. Optofluidic Fluorescent Imaging Cytometry on a Cell Phone. *Anal. Chem.* **2011**, *83*, 6641–6647.
- Zhu, H.; Yaglidere, O.; Su, T.-W.; Tseng, D.; Ozcan, A. Cost-Effective and Compact Wide-Field Fluorescent Imaging on a Cell-Phone. *Lab Chip* **2011**, *11*, 315–322.
- Zhu, H.; Sencan, I.; Wong, J.; Dimitrov, S.; Tseng, D.; Nagashima, K.; Ozcan, A. Cost-Effective and Rapid Blood Analysis on a Cell-Phone. *Lab Chip* **2013**, *13*, 1282–1288.
- Mudanyali, O.; Dimitrov, S.; Sikora, U.; Padmanabhan, S.; Navruz, I.; Ozcan, A. Integrated Rapid-Diagnostic-Test Reader Platform on a Cellphone. *Lab Chip* **2012**, *12*, 2678–2686.
- Wang, S.; Zhao, X.; Khimji, I.; Akbas, R.; Qiu, W.; Edwards, D.; Cramer, D. W.; Ye, B.; Demirci, U. Integration of Cell Phone Imaging with Microchip ELISA To Detect Ovarian Cancer HE4 Biomarker in Urine at the Point-of-Care. *Lab Chip* **2011**, *11*, 3411–3418.
- Stedtfeld, R. D.; Tourlousse, D. M.; Seyrig, G.; Stedtfeld, T. M.; Kronlein, M.; Price, S.; Ahmad, F.; Gulari, E.; Tiedje, J. M.; Hashsham, S. A. Gene-Z: A Device for Point of Care Genetic Testing Using a Smartphone. *Lab Chip* **2012**, *12*, 1454–1462.
- Preechaburana, P.; Gonzalez, M. C.; Suska, A.; Filippini, D. Surface Plasmon Resonance Chemical Sensing on Cell Phones. *Angew. Chem., Int. Ed.* **2012**, *51*, 11585–11588.
- Zhu, H.; Isikman, S. O.; Mudanyali, O.; Greenbaum, A.; Ozcan, A. Optical Imaging Techniques for Point-of-Care Diagnostics. *Lab Chip* **2013**, *13*, 51–67.
- Preechaburana, P.; Suska, A.; Filippini, D. Biosensing with Cell Phones. *Trends Biotechnol.* **2014**, *32*, 351–355.
- Walt, D. R. Fibre Optic Microarrays. *Chem. Soc. Rev.* **2010**, *39*, 38–50.
- Piepenburg, O.; Williams, C. H.; Stemple, D. L.; Armes, N. A. DNA Detection Using Recombination Proteins. *PLoS Biol.* **2006**, *4*, e204.
- Liong, M.; Hoang, A. N.; Chung, J.; Gural, N.; Ford, C. B.; Min, C.; Shah, R. R.; Ahmad, R.; Fernandez-Suarez, M.; Fortune, S. M.; et al. Magnetic Barcode Assay for Genetic Detection of Pathogens. *Nat. Commun.* **2013**, *4*, 1752.
- Yerly, S.; Quadri, R.; Negro, F.; Barbe, K. P.; Cheseaux, J. J.; Burgisser, P.; Siegrist, C. A.; Perrin, L. Nosocomial Outbreak of Multiple Bloodborne Viral Infections. *J. Infect. Dis.* **2001**, *184*, 369–372.
- Chu, C.; Hwang, S.; Luo, J.; Wang, Y.; Lu, R.; Lai, C.; Tsay, S.; Wu, J. Hepatitis C: Comparison with Acute Hepatitis B—Comparison of Clinical, Virologic and Pathologic Features in Patients with Acute Hepatitis B and C. *J. Gastroenterol. Hepatol.* **2001**, *16*, 209–214.
- Peng, X.; Schlamp, M. C.; Kadavanich, A. V.; Alivisatos, A. P. Epitaxial Growth of Highly Luminescent CdSe/CdS Core/Shell Nanocrystals with Photostability and Electronic Accessibility. *J. Am. Chem. Soc.* **1997**, *119*, 7019–7029.

34. Hines, M. A.; Guyot-Sionnest, P. Synthesis and Characterization of Strongly Luminescing ZnS-Capped CdSe Nanocrystals. *J. Phys. Chem.* **1996**, *100*, 468–471.
35. Guizar-Sicairos, M.; Thurman, S. T.; Fienup, J. R. Efficient Subpixel Image Registration Algorithms. *Opt. Lett.* **2008**, *33*, 156–158.
36. Guizar-Sicairos, M. Efficient Subpixel Image Registration by Cross-Correlation; <http://www.mathworks.com/matlabcentral/fileexchange/18401-efficient-subpixel-image-registration-by-cross-correlation>.
37. Ballard, D. H. Generalizing the Hough Transform To Detect Arbitrary Shapes. *Pattern Recognit.* **1981**, *13*, 111–122.
38. Peng, T. Detect Circles with Various Radii in Grayscale Image via Hough Transform; <http://www.mathworks.com/matlabcentral/fileexchange/9168-detect-circles-with-various-radii-in-grayscale-image-via-hough-transform>.